

Improved visibility of brain tumors in synthetic MP-RAGE anatomies with pure T_1 weighting

Ulrike Nöth^{a*}, Elke Hattingen^b, Oliver Bähr^c, Julia Tichy^c and Ralf Deichmann^a

Conventional MRI for brain tumor diagnosis employs T_2 -weighted and contrast-enhanced T_1 -weighted sequences. Non-enhanced T_1 -weighted images provide improved anatomical details for precise tumor location, but reduced tumor-to-background contrast as elevated T_1 and proton density (PD) values in tumor tissue affect the signal inversely. Radiofrequency (RF) coil inhomogeneities may further mask tumor and edema outlines. To overcome this problem, the aims of this work were to employ quantitative MRI techniques to create purely T_1 -weighted synthetic anatomies which can be expected to yield improved tissue and tumor-to-background contrasts, to compare the quality of conventional and synthetic anatomies, and to investigate optical contrast and visibility of brain tumors and edema in synthetic anatomies. Conventional magnetization-prepared rapid acquisition of gradient echoes (MP-RAGE) anatomies and maps of T_1 , PD and RF coil profiles were acquired in comparable and clinically feasible times. Three synthetic MP-RAGE anatomies (PD T_1 weighting both with and without RF bias; pure T_1 weighting) were calculated for healthy subjects and 32 patients with brain tumors. In healthy subjects, the PD T_1 -weighted synthetic anatomies with RF bias precisely matched the conventional anatomies, yielding high signal-to-noise (SNR) and contrast-to-noise (CNR) ratios. Pure T_1 weighting yielded lower SNR, but high CNR, because of increased optical contrasts. In patients with brain tumors, synthetic anatomies with pure T_1 weighting yielded significant increases in optical contrast and improved visibility of tumor and edema in comparison with anatomies reflecting conventional T_1 contrasts. In summary, the optimized purely T_1 -weighted synthetic anatomy with an isotropic resolution of 1 mm, as proposed in this work, considerably enhances optical contrast and visibility of brain tumors and edema. Copyright © 2015 John Wiley & Sons, Ltd.

Keywords: quantitative MRI (qMRI); synthetic anatomies; T_1 weighting; high-grade glioma; MP-RAGE; tumor visibility; edema visibility; optical contrast

INTRODUCTION

MRI is crucial for brain tumor diagnosis. Advanced techniques, such as MRS, perfusion mapping and diffusion-weighted imaging, may provide important information on tumor malignancy and aggressiveness, in particular on neovascularization and tumor cell proliferation. Although margin delineation of infiltrative glial tumors may benefit from advanced MRI methods, conventional MRI is still indispensable for the depiction of tumor morphology and tumor location with respect to functionally important anatomical structures. Furthermore, high-resolution conventional MRI allows the measurement of tumor dimensions and the planning of tumor biopsy, neurosurgical resection, radiosurgery and targeted radiotherapy. Images should depict the tumor with high contrast to adjacent brain structures and show clearly whether and to what extent the tumor infiltrates brain structures of critical importance with respect to neurological functions [e.g. internal capsule (IC), cortical ribbon and basal ganglia]. Different weightings are exploited for this purpose. The best tumor-to-background contrast is achieved via T_2 weighting, proton density (PD) weighting or fluid-attenuated inversion recovery (FLAIR) (1). The best contrast between white matter (WM) and gray matter (GM) for the investigation of brain anatomy is provided by T_1 -weighted sequences, such as three-dimensional (3D) magnetization-prepared rapid acquisition of gradient echoes (MP-RAGE) (2,3). Furthermore, 3D imaging with isotropic voxel

* Correspondence to: U. Nöth, Brain Imaging Center, University Hospital, Schleusenweg 2–16, 60528 Frankfurt, Germany.
E-mail: noeth@med.uni-frankfurt.de

a U. Nöth, R. Deichmann
Brain Imaging Center, Goethe University Frankfurt, Frankfurt/Main, Germany

b E. Hattingen
Department of Neuroradiology, Goethe University Frankfurt, Frankfurt/Main, Germany

c O. Bähr, J. Tichy
Dr Senckenberg Institute of Neurooncology, Goethe University Frankfurt, Frankfurt/Main, Germany

Abbreviations used: 2D/3D, two-/three-dimensional; α , flip angle; aMPR, acquired MP-RAGE; B_1 , transmit sensitivity profile; CA, contrast agent; CN, caudate nucleus; CNR, contrast-to-noise ratio; CSF, cerebrospinal fluid; EPI, echo planar imaging; ES, echo spacing; FGM, frontal GM; FLAIR, fluid-attenuated inversion recovery; FLASH, fast low-angle shot; FOV, field of view; FWM, frontal WM; GE, gradient echo; GM, gray matter; IC, internal capsule; IR, inversion recovery; MP-RAGE, magnetization-prepared rapid acquisition of gradient echoes; OWM, occipital WM; PA, pallidum; PD, proton density; PE, phase encoding; PU, putamen; qMRI, quantitative MRI; RF, radiofrequency; ROI, region of interest; RP, receive sensitivity profile; SNR, signal-to-noise ratio; sMPR, synthetic MP-RAGE with PD T_1 weighting and RF bias; sMPR_PD_T1, synthetic MP-RAGE with PD T_1 weighting but without RF bias; sMPR_T1, synthetic MP-RAGE with pure T_1 weighting; TI, inversion time; VFA, variable flip angle; WM, white matter.

sizes enables multi-planar reformatting in different orientations, thus reducing the number of required scans. However, to accentuate the tumor tissue itself, T_1 weighting is, in general, inferior to T_2 weighting (4,5), unless a contrast agent (CA) is applied for tumor enhancement. This constitutes a clear drawback, as T_1 -weighted images have the advantage of showing tumor locations with improved anatomical details.

The question arises as to why T_2 weighting outperforms T_1 weighting in terms of brain tumor visibility. As T_1 , T_2 and PD are increased in tumor tissue (6–8), tumors appear hyperintense in T_2 -weighted images, as both PD and T_2 increase the local signal. In contrast, T_1 prolongation yields signal hypointensity; therefore, in T_1 -weighted sequences, T_1 and PD inversely influence the signal, thus masking their respective weightings and reducing tumor and edema visibility. Furthermore, intensity variations caused by non-uniformities of the radiofrequency (RF) coil sensitivity profiles may further reduce the visibility of brain pathologies.

To overcome the antagonism of PD and T_1 weighting and to reduce the RF coil bias, the interleaved acquisition of an MP-RAGE and an additional gradient echo (GE) dataset, followed by quotient formation, has been proposed, thus eliminating the PD influence and yielding purely T_1 -weighted images with improved anatomical contrast (9). Similarly, the MP2RAGE sequence (10) combines two simultaneously acquired MP-RAGE (aMPR) images with different inversion times (TIs), eliminating PD weighting and reducing RF coil bias. In a clinical study performed on patients with multiple sclerosis (11), MP2RAGE outperformed conventional MP-RAGE in terms of both lesion count and lesion volume determination.

Quantitative MRI (qMRI) techniques aim to yield the direct determination of tissue parameters and RF coil profiles. Several T_1 mapping methods employ the variable flip angle (VFA) approach (12), which also allows for the mapping of PD and RF coil profiles (13). The knowledge of tissue parameters enables the construction of synthetic MR images with arbitrary contrasts (14). As an example, synthetic T_1 -weighted anatomies without any PD bias were calculated from VFA data, improving image contrasts (15). Thus, it is likely that purely T_1 -weighted synthetic MP-RAGE images allow for improved tumor detection. Furthermore, the absence of any RF coil bias increases data comparability in multi-center studies (15).

In the first part of this study, qMRI and standard MP-RAGE data with comparable scan durations were acquired on healthy subjects, and three synthetic MP-RAGE anatomies (PD T_1 weighting both with and without RF coil bias, pure T_1 weighting) were calculated. The goals of this part of the study were as follows.

- (1) To test how closely standard MP-RAGE anatomies match the respective synthetic data.
- (2) To compare the signal-to-noise ratios (SNRs), contrast-to-noise ratios (CNRs) and optical contrasts for standard and synthetic anatomies, the optical contrast being defined as the signal difference between two areas, divided by their signal average (16).

In the second part of the study, the same qMRI protocol was applied to patients with brain tumors with the following goals.

- (1) To compare optical contrasts between tumor tissue, edema and surrounding normal tissue for the three synthetic anatomies.
- (2) To rate the synthetic anatomies in terms of visibility and delineation of pathologic tissue.

METHODS

Subjects

For the first part of this study, qMRI and standard MP-RAGE data were acquired on eight healthy subjects (four women; age range, 27–57 years; mean age, 33 years). The study was approved by the ethics committee of the University Hospital Frankfurt. Written informed consent was obtained from all subjects before participation.

For the second part of this study, the same qMRI protocol was performed on 32 patients (13 women; age range, 26–88 years; mean age, 59 years) with a suspected diagnosis of high-grade glioma on the basis of previous conventional diagnostic MRI scans (generally performed off-site as most patients were transferred to the University Hospital Frankfurt after primary diagnosis). Patients were screened before any intervention. A high-grade glioma was subsequently confirmed in all patients via histopathology. It should be noted that this prospective study was part of a more comprehensive study, employing multi-parameter mapping for the assessment of correlations between MR-accessible tissue parameters and histopathological and immunohistochemical data. The patient study was also approved by the ethics committee of the University Hospital Frankfurt. Written informed consent was obtained from all patients before participation.

General description of the MP-RAGE sequence

The MP-RAGE sequence acquires $N_{2D} \times N_{3D}$ pixels in the 2D and 3D phase-encoding (PE) directions and consists of blocks with the structure: [$180^\circ - \tau_1$ — acquisition — τ_2]. During acquisition, N_{3D} GEs with different 3D PE are acquired with a nominal excitation angle α and echo spacing (ES, time difference between excitation pulses). The k -space center is covered after n_1 echoes (generally $N_{3D}/2$). TR is the block duration and is thus given by $TR = \tau_1 + ES \cdot N_{3D} + \tau_2$. As N_{2D} blocks with different 2D PE are acquired, the scan duration is $TR \cdot N_{2D}$. TI is the time difference between inversion and k -space center coverage, and is thus given by $TI = \tau_1 + ES \cdot n_1$. The sequence is fully defined by the independent parameters [TR, TI, ES, α , n_1 , N_{2D} , N_{3D}].

The longitudinal relaxation is governed by T_1 during τ_1 and τ_2 , and by

$$T_1^* = [1/T_1 - 1/ES \cdot \ln(\cos(\alpha \cdot B_1))]^{-1} \quad [1]$$

during acquisition (17). In this equation, B_1 is the transmit sensitivity profile of the RF coil. B_1 is given in relative units, assuming unity where the actual angle matches the nominal value.

With the parameters

$$E_1 = \exp(-\tau_1/T_1) \quad E_2 = \exp(-\tau_2/T_1) \quad (2a)$$

$$E_3 = \exp(-(N_{3D} \cdot ES)/T_1^*) \quad E_4 = \exp(-(n_1 \cdot ES)/T_1^*) \quad (2b)$$

the MP-RAGE image signal can be calculated as (18):

$$S = M_0 \cdot \sin(\alpha \cdot B_1) \cdot RP \cdot Q \quad (3a)$$

where Q is given by:

$$Q = \frac{E_4 \cdot [1 - 2 \cdot E_1 + E_1 \cdot E_2] + \frac{T_1^*}{T_1} \cdot [1 + E_1 \cdot E_2 \cdot E_3 - E_1 \cdot E_2 \cdot E_4 - E_4]}{1 + E_1 \cdot E_2 \cdot E_3} \quad (3b)$$

In these equations, M_0 is the equilibrium magnetization (which is proportional to PD) and RP is the receive sensitivity profile of the RF coil.

Acquisition of MR data

Measurements were performed on two different 3-T whole-body MR scanners (Siemens Medical Solutions, Erlangen, Germany), both equipped with a body coil for RF transmission and an eight-channel phased-array head coil for signal reception. Healthy subjects were scanned on a Magnetom TRIO and patients on a Magnetom VERIO system. The following data were acquired for each subject/patient.

Acquisition 1: MP-RAGE (aMPR) (healthy subjects only)

Parameters were chosen as described in ref. (19): field of view (FOV), 256 mm (readout, inferior–superior) \times 224 mm (posterior–anterior) \times 160 mm (left–right), matrix 256 \times 224 \times 160; TR/TE/TI/α = 2420 ms/3.68 ms/960 ms/9°; ES = 10.2 ms; bandwidth, 140 Hz/pixel; N_{2D} = 224; N_{3D} = 160; n_1 = 80; duration, 9 min 6 s.

Acquisition 2: T_1 and PD mapping

Mapping was based on the VFA technique, acquiring a PD-weighted and a T_1 -weighted spoiled fast low-angle shot (FLASH) dataset using different excitation angles α_1 and α_2 . The imaging parameters were as follows: FOV and matrix as above; TR/TE/ α_1/α_2 = 16.4 ms/6.7 ms/4°/24°; bandwidth, 222 Hz/pixel. To improve the SNR, a FLASH-echo planar imaging (EPI) hybrid readout (20) was used, acquiring two GEs with different PE per excitation. The total acquisition time for both datasets was 9 min and 48 s.

Acquisition 3: B_1 mapping

The B_1 mapping method described in ref. (21) was used, acquiring two GE datasets, the second being preceded by an RF pulse which rotates the magnetization vector by an angle β (nominal value $\beta_0 = 45^\circ$), followed by a crusher gradient to suppress transverse magnetization. As the acquisition employs centric PE, the signal represents the initial longitudinal magnetization, and so the quotient of both images yields $\cos(\beta)$ and B_1 follows from β/β_0 . As B_1 varies smoothly, an isotropic spatial resolution of 4 mm was chosen, using the same FOV as above with a matrix of 64 \times 56 \times 40; further parameters were as follows: TR/TE/α = 11 ms/5 ms/11°; bandwidth, 260 Hz/pixel; duration, 53 s.

Acquisition 4: additional data (patients only)

As described above, this study was part of a more comprehensive qMRI study, comprising T_2 mapping by acquiring five T_2 -weighted datasets with different TEs (16, 64, 96, 128 and 176 ms). Further parameters were as follows: FOV, 240 \times 180 mm²; matrix, 192 \times 144; 25 axial slices (2 mm, no inter-slice gap); TR = 4670 ms; bandwidth, 100 Hz/pixel. Furthermore, T_1 mapping was repeated after CA administration. For this study, only the T_2 -weighted dataset with TE = 96 ms and the T_1 -weighted dataset after CA administration were used to select the regions of interest (ROIs) (see below).

In addition, for two selected patients, data were compared with images obtained for primary diagnosis, namely FLAIR, T_2 weighting and T_1 weighting after CA administration. As these

data were acquired off-site and only served for comparison, the parameters are not listed.

Data post-processing and analyses

Tissue segmentation and data co-registration were performed with the FMRIB Software Library (FSL, <http://www.fmrib.ox.ac.uk/fsl>). All ROIs for data analyses were selected manually with MRICRON (<http://www.mccauslandcenter.sc.edu/mricro/mricon/>). Data post-processing and analyses were performed with custom-built programs written in MatLab (MathWorks, Natick, MA, USA).

Post-processing 1: co-registration and segmentation

To account for subject motion, MP-RAGE and PD-weighted data were co-registered to the T_1 -weighted data. Tissue masks for WM, GM and cerebrospinal fluid (CSF) were obtained by segmentation of T_1 -weighted data and the application of a threshold of 0.999 to the resulting probability maps.

Post-processing 2: B_1 and T_1 mapping

B_1 was evaluated according to ref. (21), as described above. Correction for T_1 relaxation effects during the acquisition was performed tissue-wise, assuming T_1 values of 900, 1400 and 4500 ms in WM, GM and CSF, respectively (21). T_1 maps were obtained via VFA analysis (12): if S_i and α_i are the local signal and excitation angle in the two datasets ($i = 1, 2$), plotting of $S_i/\sin(\alpha_i)$ versus $S_i/\tan(\alpha_i)$ yields the slope $\exp(-\text{TR}/T_1)$ and thus T_1 (12). The analysis included corrections for B_1 inhomogeneities, assuming for each pixel the actual excitation angle $\alpha = B_1 \cdot \alpha_{\text{nominal}}$ (22). Furthermore, T_1 maps were corrected for insufficient spoiling of transverse magnetization (22).

Post-processing 3: PD mapping

PD maps were calculated as proposed in ref. (13). First, the PD-weighted data were corrected for T_1 bias, yielding maps of $M_0 = \text{PD} \cdot \text{RP}$. Subsequently, 'pseudo PD values' were calculated via $1/\text{PD}_{\text{pseudo}} = A + B/T_1$ with $A = 0.858$ and $B = 522$ ms, which closely match real PD values in WM and GM (13); therefore, the quotient of M_0 and $\text{PD}_{\text{pseudo}}$ yields an estimate for RP ($\text{RP}_{\text{estimate}}$). A smooth RP map was calculated from $\text{RP}_{\text{estimate}}$ via polynomial fitting of sixth order. PD follows from M_0/RP , approximately scaled to unity in CSF. It should be noted that an accurate determination of PD would involve a T_2^* correction as a result of the finite TE of 6.7 ms, requiring additional data (23). However, in this study, the goal was the comparison of synthetic MP-RAGE anatomies with standard anatomies acquired with a finite TE of 3.7 ms. The residual TE difference of $\Delta\text{TE} = 3$ ms yields minor signal losses in the synthetic anatomies of about 6% (WM) and 4% (GM), assuming T_2^* values of 50 and 70 ms, respectively (23). As the term $\exp(-\Delta\text{TE}/T_2^*)$ is almost identical for WM and GM, with a relative difference of 1.7% only, additional T_2^* contrasts in the synthetic data are negligible. As a result of these considerations and the fact that the method was applied on tumor patients with the requirement of keeping the experiment duration as short as possible, T_2^* corrections were omitted.

Post-processing 4: calculation of synthetic anatomies

Based on the maps of T_1 , PD, B_1 and RP, three synthetic MP-RAGE anatomies were calculated from Equation [3a] with Q given by Equation [3b] in combination with Equations [1] and [2].

- (1) Synthetic MP-RAGE with PD T_1 weighting and RF coil bias (sMPR), assuming $M_0 = \text{PD}$ and using the measured B_1 and RP maps: $S(\text{sMPR}) = \text{PD} \cdot \sin(\alpha \cdot B_1) \cdot \text{RP} \cdot Q(T_1, \alpha \cdot B_1)$.
- (2) Synthetic MP-RAGE with PD T_1 weighting, but without RF coil bias (sMPR_PD_T1), assuming $M_0 = \text{PD}$, $B_1 = 1$, RP = 1: $S(\text{sMPR_PD_T1}) = \text{PD} \cdot \sin(\alpha) \cdot Q(T_1, \alpha)$.
- (3) Synthetic MP-RAGE with pure T_1 weighting (sMPR_T1), assuming $M_0 = 1$, $B_1 = 1$, RP = 1: $S(\text{sMPR_T1}) = \sin(\alpha) \cdot Q(T_1, \alpha)$.

Furthermore, for two patients, synthetic inversion recovery (IR) images were calculated from $S(\text{IR}) = |1 - 2 \times \exp(-\text{TI}/T_1)|$, assuming TI of 500, 1100 or 2000 ms.

Post-processing 5: calculation of noise maps (healthy subjects only)

The noise σ in all acquired datasets was determined from the signal inside ROIs in the image background, i.e. in regions outside of the subject where the signal is solely governed by system noise. As these data are derived from modulus images, the true noise can be obtained by dividing the standard deviation of this background signal by a Rayleigh factor of 0.701 (24). For further analysis, it must be taken into account that there are two types of dataset: 'acquired datasets' (such as aMPR and the PD- and T_1 -weighted data) and 'derived datasets' (such as the T_1 and PD maps and all synthetic anatomies). For the acquired datasets, the noise σ can be obtained as explained above and represents directly the image noise. For the derived datasets, image noise must be calculated from the noise in the underlying acquired data, using the laws of error propagation: if x_1 and x_2 are local signal intensities in the PD- and T_1 -weighted datasets, respectively, the local signal (y) in any derived dataset is a function $y(x_1, x_2)$. Thus, noise in the derived dataset is given by:

$$\sigma_y = \sqrt{\left(\frac{\partial y}{\partial x_1}\right)^2 \cdot \sigma_{x_1}^2 + \left(\frac{\partial y}{\partial x_2}\right)^2 \cdot \sigma_{x_2}^2} \quad (4)$$

In Equation [4], σ_{x_1} and σ_{x_2} are the noise levels in the PD- and T_1 -weighted datasets, respectively. As both datasets were acquired with identical matrix size and receiver band width, the noise levels can be assumed to be identical: for the healthy subjects, the average relative difference between σ_{x_1} and σ_{x_2} was only $0.96 \pm 0.72\%$, and so Equation [4] was simplified by using an identical value σ_x .

In theory, the derivatives can be obtained analytically from Equations [1–3]. However, because of the complexity of Equation [3], a numerical calculation was preferred. The derived data were first calculated from the acquired data, yielding values $y_1 = y(x_1, x_2)$. Subsequently, the values of the first input dataset were increased by Δx , yielding the modified derived data $y_2 = y(x_1 + \Delta x, x_2)$. From $\Delta y = y_2 - y_1$, the first derivative $\partial y / \partial x_1$ is approximately given by $\Delta y / \Delta x$. The second derivative is obtained similarly, and noise in the derived data follows from Equation [4]. This procedure was performed to obtain noise maps for the T_1 map, PD map and the three synthetic MP-RAGE anatomies. The value of Δx should be sufficiently small so that the

quotient $\Delta y / \Delta x$ yields a good estimate of the respective derivative. In this study, Δx was chosen to amount to 5% of x_1 or x_2 .

Analyses: healthy subjects

Acquired and synthetic MP-RAGE anatomies were compared with the following goals.

- (1) To test whether sMPR yields the same signal and contrast characteristics as aMPR.
- (2) To compare the SNR, CNR and optical image contrast values that are achieved in or between different brain areas in the various synthetic anatomies with those in aMPR.

Data acquisition and post-processing were performed as explained above. The following data analysis steps were performed for each single subject; the respective results were then averaged across subjects.

- (1) Noise in the T_1 and PD maps was averaged across WM and GM masks to assess the respective measurement precision. It should be noted that this analysis considers SNR limitations in the acquired datasets imposed by thermo-noise, but not the effects of physiological noise (such as subject movement).
- (2) To test how well aMPR is replicated by sMPR, the quotient of both datasets was calculated and averaged separately across WM and GM masks.
- (3) For aMPR and all synthetic anatomies, SNR was determined in several ROIs, located in the frontal WM (FWM), frontal GM (FGM), occipital WM (OWM), caudate nucleus (CN), putamen (PU), pallidum (PA) and IC. SNR values were calculated by dividing the respective image data either by the noise value (aMPR) or the noise map (synthetic anatomies).
- (4) Optical contrast and CNR values were determined between the following pairs of ROIs, FWM–FGM, FWM–CN, PU–PA, PA–IC, and compared between aMPR and synthetic anatomies. For aMPR, CNR followed from the respective SNR differences. For the synthetic anatomies, CNR was obtained by dividing the signal difference by an average noise value $\langle \sigma \rangle$, given by (15):

$$\langle \sigma \rangle = \sqrt{\frac{\sigma_1^2 + \sigma_2^2}{2}} \quad [5]$$

where σ_1 and σ_2 are the noise values in the respective ROIs.

The optical contrast between two ROIs was calculated from the signal difference, divided by the signal average (16).

Analyses: patients with tumors

The purpose of the patient study was to identify the synthetic anatomy best suited for differentiation between tumor-related tissue changes and healthy brain tissue with special regard to functionally relevant structures, such as the basal ganglia. Thus, only acquisitions 2–4 described above were performed, reducing the scan duration for patients. No noise maps were calculated as the analysis was based on optical contrast values (see above), rather than on SNR and CNR. For each patient, ROIs were selected in pathological areas and adjacent healthy tissue, and optical contrasts were determined for one or more of the following cases: (i) between tumor and adjacent functionally relevant normal tissue; (ii) between edema and adjacent normal tissue; (iii) between tumor and edema. ROIs were manually chosen and

mutually exclusive in tumor tissue, in edema and in the respective adjacent normal-appearing brain, based on the T_2 -weighted ($TE = 96$ ms) and contrast-enhanced T_1 -weighted images from the quantitative T_1 and T_2 MR protocol, which were acquired in the same session and co-registered. To define edema ROIs, imaging criteria as described previously were used (25). Tumor ROIs were placed in solid masses free of necrosis which were enhanced in T_1 -weighted images and/or in areas with a clear pattern of infiltrative tumor (26), selecting the most critical areas of the tumor with respect to brain function, i.e. areas abutting or infiltrating the basal ganglia or the cortical ribbon. Being aware that a clear distinction between tumor, edema and 'normal tissue' is principally not possible in infiltrative brain tumors, the ROIs were not placed in areas with ambiguous imaging features. In particular, some tumors displayed no clear edema, but rather widespread tumor infiltration. In these cases, no edema ROI was defined. In addition, some tumors were surrounded by edema, and so a normal tissue ROI adjacent to the tumor could not be defined.

Optical contrast values between tumor and adjacent normal tissue (T-N), edema and adjacent normal tissue (E-N) and tumor and edema (T-E) were calculated for each of the three synthetic anatomies, and the underlying quantitative T_1 and PD maps for comparison. Pair-wise comparisons between the different synthetic anatomies (i.e. sMPR_T1 versus sMPR and sMPR_T1 versus sMPR_PD_T1) were conducted via paired *t*-tests.

Two experienced neuroradiologists rated independently for each patient the three synthetic anatomies (presented in randomized order) in terms of visibility and delineation of pathologic areas. Both neuroradiologists were blinded to the patients and unaware of the respective conventional images, with access to the synthetic data only, and permission to adapt brightness and contrast. A score of '1' was given for the synthetic anatomy with the worst, '2' with intermediate and '3' with best contrast for visibility and delineation.

RESULTS

Healthy subjects

Average T_1 values were 900.0 ± 33.6 ms (WM) and 1562.9 ± 40.1 ms (GM). The respective noise values were 25.6 ± 1.5 ms (WM) and 51.4 ± 2.9 ms (GM). Average PD values were 69.4 ± 1.3 pu (WM) and 85.5 ± 0.7 pu (GM). The respective noise values were 1.3 ± 0.1 pu (WM) and 1.7 ± 0.1 pu (GM).

Figure 1 shows single slices of (from left to right) aMPR, sMPR, sMPR_PD_T1 and sMPR_T1 for four representative subjects. The striking similarity between aMPR and sMPR is reconfirmed by the quotient of both datasets, which yielded average values of 0.978 ± 0.010 (WM) and 0.971 ± 0.010 (GM). Thus, it can be stated that the theory presented above allows for close replication of aMPR data. According to Table 1, the SNR in sMPR attains about 90% of the SNR in aMPR in WM, about 82% in FGM and about 76% in deep brain structures (CN, PU, PA). Removing the RF coil bias does not significantly affect the SNR values. In contrast, the SNR in sMPR_T1 is decreased, attaining about 50–55% of the SNR in aMPR.

Table 2 shows that CNR values between most brain structures are about 20% lower in sMPR than in aMPR, concomitant with the SNR reductions. However, sMPR_T1 maintains relatively high CNR values, in spite of reduced SNR, preserving levels between 79% and 95% of the CNR values in aMPR. This table also shows

the respective optical contrast values which are similar for aMPR and sMPR, again indicating that the algorithm replicates closely aMPR data. For sMPR_T1, contrasts are increased considerably, which is obviously the reason for the phenomenon described above (high CNR in spite of reduced SNR).

Patients with tumors

ROI-based optical contrast analysis

Six of 32 patients were excluded from the ROI-based optical contrast analysis: three as a result of severe movement artifacts, one because of extensive tumor hemorrhage yielding T_1 shortening (hyperintensity in T_1 -weighted images), one as a result of severe artifacts from a fixed dental prosthesis, and one because of diffuse gliomatosis without clear edema, impairing reliable tumor and edema margin delineation. In the latter, the patient was included in the visual analysis, but excluded from quantitative evaluation. In 18 of the remaining 26 patients, tumor tissue abutted normal-appearing brain tissue; in 17 of these, critical brain structures, such as the basal ganglia with IC ($n = 16$) or IC alone ($n = 1$), were reached or even infiltrated; one abutted WM only. Figure 2 shows single slices (isotropic resolution, 1 mm) of (from left to right) sMPR, sMPR_PD_T1 and sMPR_T1 for four patients. sMPR_T1 (last column) yields the best delineation of the tumor. Row 1 shows an intraventricular glioma trapping the temporal horn and infiltrating the midbrain and thalamus (arrow). Row 2 shows a tumor infiltrating the basal ganglia and hypothalamus (arrows) with the tumor contrasting with the adjacent brain only in sMPR_T1. Row 3 shows a glioblastoma infiltrating the insula and the basal ganglia with the tumor margin to the IC best delineated in sMPR_T1 (arrow). Row 4 shows a glioblastoma of the corpus callosum infiltrating adjacent WM and reaching the dorsal insula and thalamus (arrows).

Thirteen cases showed tumor edema which, in 11 cases, bordered on normal-appearing WM. Figure 3 shows single slices (isotropic resolution, 1 mm) of (from left to right) sMPR, sMPR_PD_T1 and sMPR_T1 for four patients. Row 1 shows a tumor edema reaching the insula, IC and external capsule (arrows). Note the small rim of edema in the anterior limb of the IC visible only in sMPR_T1. In row 2, only sMPR_T1 clearly reveals the WM edema (arrows) of a glioblastoma of the splenium (not shown). Row 3 shows the margins of a large tumor edema which can be clearly seen on sMPR_T1 despite reduced image quality from motion artifacts. Row 4 shows a technically interesting case: because of the patient's physique, the head coil was not closed properly, incapacitating the anterior phased-array elements, yielding severe signal non-uniformities (left, arrow). Nevertheless, in sMPR_PD_T1 (center) and sMPR_T1 (right), this effect is fully compensated for (albeit with local SNR reductions), and the outlines of the edema (arrow) can be clearly delineated. Also note the infiltration of the thalamus (arrowhead) visible only in sMPR_T1.

In 13 of the 26 patients, no clear edema was visible, but, in some cases, signal changes around the tumor were suspicious for infiltrative tumor on conventional MRI. Interestingly, these areas also displayed a better visibility on sMPR_T1 than on sMPR during visual rating.

Figures 4 and 5 allow for a comparison of the delineation between tumor, peritumoral edema and healthy tissue for the following imaging modalities: quantitative T_1 and PD maps (row 1), the synthetic MP-RAGE images calculated from these maps (row 2; same order as in Figs. 2 and 3), synthetic IR images

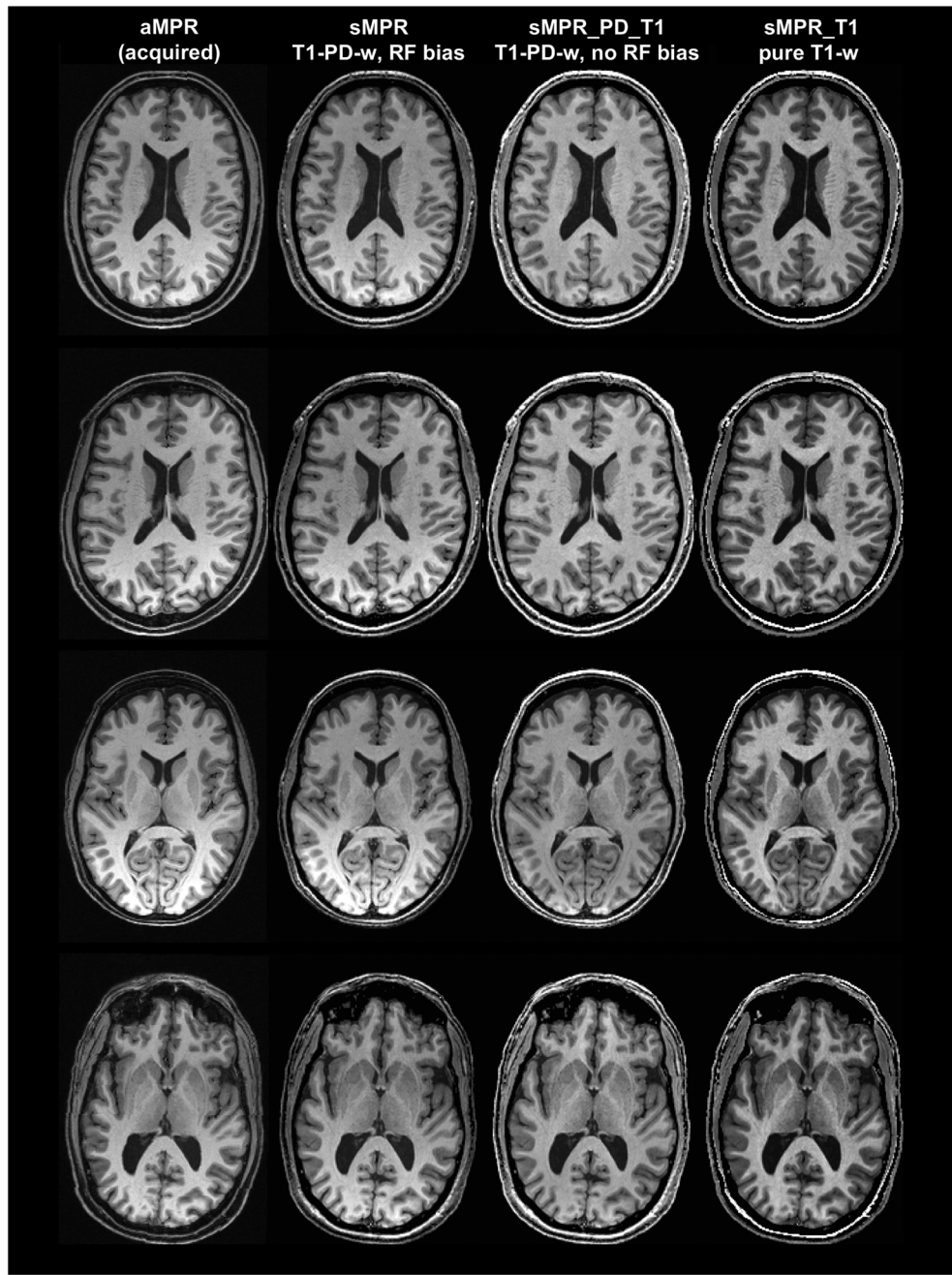


Figure 1. Single slices of the acquired and synthetic anatomies for four representative subjects. aMPR (first column) is closely replicated by sMPR (second column); the third column shows sMPR_PD_T1 and the last column shows sMPR_T1, providing best contrasts for deep brain structures. aMPR, acquired magnetization-prepared rapid acquisition of gradient echoes (MP-RAGE); sMPR, synthetic MP-RAGE with proton density (PD) T_1 weighting and radiofrequency (RF) bias; sMPR_PD_T1, synthetic MP-RAGE with PD T_1 weighting without RF bias; sMPR_T1, synthetic MP-RAGE with pure T_1 weighting.

for TI values of 500, 1100 and 2000 ms (row 3), and the conventional diagnostic images T_2 -weighted, FLAIR and T_1 -weighted after CA (row 4). The patient shown in Fig. 4 suffered from a tumor with adjacent peritumoral edema in the temporal lobe. The tumor mass showed enhancement after application of CA in the diagnostic T_1 -weighted image (arrow) and slight signal reduction relative to the edema in the diagnostic T_2 -weighted image (arrow). In the FLAIR image (which was acquired after application of CA), the margin between the tumor mass and peritumoral edema is not well defined, whereas sMPR_T1 clearly shows a border between the tumor mass and peritumoral edema (arrow). The sMPR_T1 image also delineates the affection of the IC and

the basal ganglia (arrowhead), which is also seen in the T_2 -weighted image. In contrast, anatomical details are not well discriminated on diagnostic FLAIR and contrast-enhanced T_1 -weighted images. The T_1 map and the synthetic IR images also allow a clear differentiation between solid tumor and edema, with the best contrast for TI = 2000 ms. It should be noted that all images in this figure are co-registered to the diagnostic T_2 -weighted image, resulting in an effective slice thickness of 3 mm. Figure 5 shows a patient with a glioblastoma in frontal WM that infiltrates the corpus callosum and is surrounded by edema. The T_1 map reveals that the margin of the solid tumor differs from adjacent edema, giving rise to the contrasts in

Table 1. Signal-to-noise ratios (SNRs) in frontal white matter (FWM), frontal gray matter (FGM), occipital white matter (OWM), caudate nucleus (CN), putamen (PU), pallidum (PA) and internal capsule (IC) for all anatomical sequences (averages and standard deviations across all subjects)

	aMPR	sMPR (bias)	sMPR_PD_T1 (no bias)	sMPR_T1 (T_1 only)
FWM	64.92 ± 2.32	57.27 ± 2.37	58.20 ± 2.40	34.46 ± 1.20
FGM	41.14 ± 1.19	33.45 ± 0.98	34.30 ± 1.62	24.25 ± 1.06
OWM	79.82 ± 5.77	72.03 ± 6.72	72.04 ± 6.61	43.04 ± 3.35
CN	49.25 ± 2.37	37.42 ± 1.65	34.95 ± 1.71	24.53 ± 1.16
PU	54.24 ± 3.53	41.02 ± 3.31	38.54 ± 3.17	26.67 ± 1.99
PA	61.81 ± 3.30	47.30 ± 3.39	44.22 ± 3.14	29.29 ± 1.98
IC	65.50 ± 3.05	54.26 ± 3.19	50.91 ± 2.97	32.62 ± 1.76

aMPR, acquired magnetization-prepared rapid acquisition of gradient echoes (MP-RAGE); sMPR, synthetic MP-RAGE with proton density (PD) T_1 weighting and radiofrequency (RF) bias; sMPR_PD_T1, synthetic MP-RAGE with PD T_1 weighting without RF bias; sMPR_T1, synthetic MP-RAGE with pure T_1 weighting.

Table 2. Contrast-to-noise ratios (CNRs) and optical contrast between different anatomical regions for all anatomical sequences (averages and standard deviations across all subjects)

	aMPR	sMPR (bias)	sMPR_PD_T1 (no bias)	sMPR_T1 (T_1 only)
CNR	FWM–FGM	23.78 ± 1.41	19.29 ± 1.31	18.94 ± 1.83
	FWM–CN	15.67 ± 1.97	12.20 ± 1.25	11.61 ± 1.29
	PU–PA	7.57 ± 1.09	4.47 ± 1.21	4.68 ± 0.54
	PA–IC	3.69 ± 0.72	4.90 ± 1.14	3.70 ± 0.99
Optical contrast	FWM–FGM	0.45 ± 0.02	0.43 ± 0.02	0.42 ± 0.03
	FWM–CN	0.27 ± 0.04	0.26 ± 0.03	0.26 ± 0.03
	PU–PA	0.13 ± 0.02	0.10 ± 0.03	0.11 ± 0.02
	PA–IC	0.06 ± 0.01	0.10 ± 0.03	0.08 ± 0.02

aMPR, acquired magnetization-prepared rapid acquisition of gradient echoes (MP-RAGE); sMPR, synthetic MP-RAGE with proton density (PD) T_1 weighting and radiofrequency (RF) bias; sMPR_PD_T1, synthetic MP-RAGE with PD T_1 weighting without RF bias; sMPR_T1, synthetic MP-RAGE with pure T_1 weighting.

CN, caudate nucleus; FGM, frontal gray matter; FWM, frontal white matter; IC, internal capsule; PA, pallidum; PU, putamen.

sMPR_T1, where the tumor margins are best depicted (white arrows). In contrast, the tumor margin is less pronounced on sMPR_PD_T1 and the diagnostic T_2 -weighted image, and cannot be discerned from adjacent edema on the conventional FLAIR image. Again, the synthetic IR images allow a clear differentiation between marginal solid tumor and edema, with the best contrast for TI = 1100 ms. Despite the peritumoral edema, the cortical ribbon (arrowhead) and basal ganglia (black arrow) are still visible on sMPR_T1. Furthermore, discrimination between the necrotic tumor center and the more solid tumor margin (enhancing after CA in the conventional T_1 -weighted image) is best depicted on sMPR_T1 and synthetic IR images for TI values of 500 and 2000 ms. It should be noted that the patient received glucocorticoids after off-site primary diagnostic MRI, and so edema and mass effect are reduced in quantitative and synthetic data as they were acquired 10 days later. All images in this figure are co-registered to the diagnostic T_2 -weighted image, resulting in an effective slice thickness of 6 mm.

Figure 6 shows average optical contrast values for the different adjacent regions (T–N, E–N, T–E) for all synthetic anatomies and the underlying quantitative T_1 and PD maps. sMPR_T1 provides significantly higher contrasts than the other synthetic anatomies,

both between tumor and surrounding normal tissue (increase of about 50%) and between edema and surrounding normal tissue. For the contrast between tumor and edema, there is a trend towards improvements in sMPR_T1, which, however, does not attain a level of significance. Nevertheless, it should be noted that, in all synthetic anatomies, the contrast between tumor and edema is high, matching approximately the contrast between tumor and surrounding normal tissue (see Fig. 6). The optical contrast values for the quantitative T_1 map are very similar to those of sMPR_T1 (ca. 10% lower), whereas the optical contrast values for the quantitative PD map are considerably lower.

Visual rating analysis

Four patients were excluded from visual rating (three as a result of severe motion artifacts and one because of extensive tumor hemorrhage), whereas one patient with less severe motion artifacts (Fig. 3, row 3) and the patient with gliomatosis were included, yielding a total number of $n = 28$ for visual rating.

For all evaluated patients, both neuroradiologists rated sMPR_T1 as the best choice concerning the visibility of pathologies. For 22 of the 28 evaluated patients, both neuroradiologists

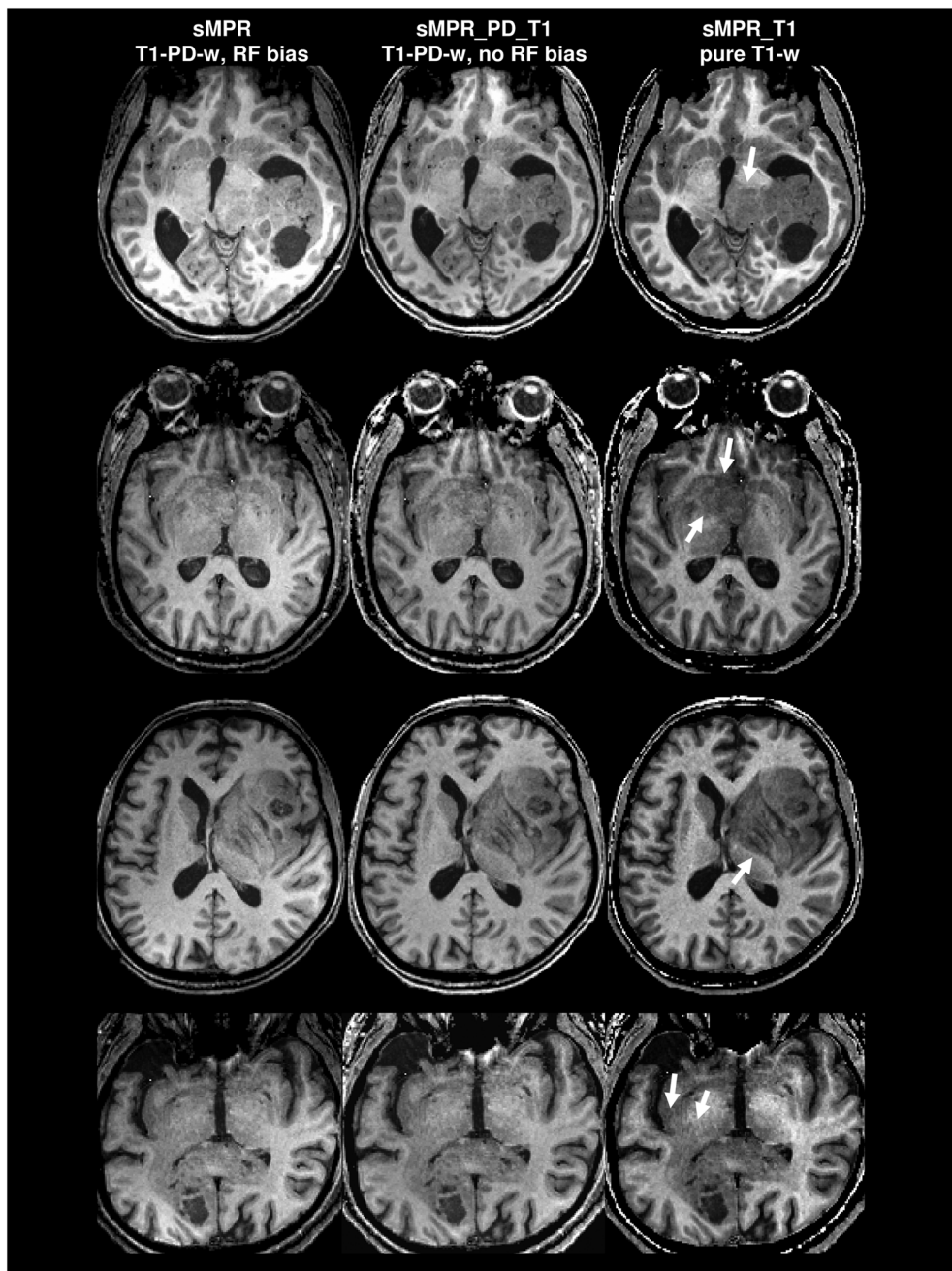


Figure 2. Single slices of the synthetic magnetization-prepared rapid acquisition of gradient echoes (MP-RAGE) anatomies for four patients. First column, with proton density (PD) T_1 weighting and radiofrequency (RF) bias (this anatomy replicates a standard acquired MP-RAGE); second column, with PD T_1 weighting and no RF bias; last column, with pure T_1 weighting, providing the best contrasts for tumor delineation (arrows).

rated sMPR_PD_T1 to be the second-best choice. These results match the findings above, according to which sMPR_T1 provides improved contrast, whereas the contrast differences between sMPR_PD_T1 and sMPR are rather marginal. This is reflected in the total scores of 84/84 (first/second neuroradiologist) for sMPR_T1, 53/51 for sMPR_PD_T1 and 31/33 for sMPR.

DISCUSSION

This study shows that synthetic MP-RAGE images free of RF coil bias and PD weighting (sMPR_T1) improve the visual delineation of high-grade gliomas from normal brain, especially in

functionally critical brain structures, such as the basal ganglia (Fig. 2). This is a result of the significantly higher optical contrast (about 50% increase) in sMPR_T1 relative to the synthetic anatomies comprising T_1 and PD weighting, both with (sMPR) and without (sMPR_PD_T1) RF coil bias. Significant optical contrast enhancement was observed between tumor and normal brain, as well as between edema and normal brain, but not between tumor and edema (Fig. 6). The relatively small optical contrast enhancement between tumor and edema in sMPR_T1 may be a result of the tumor biology, as there is an intermediate transition zone in which tumor cells infiltrate into the edema. In contrast, the delineation of the tumor from functionally important brain structures may be crucial for treatment decisions.

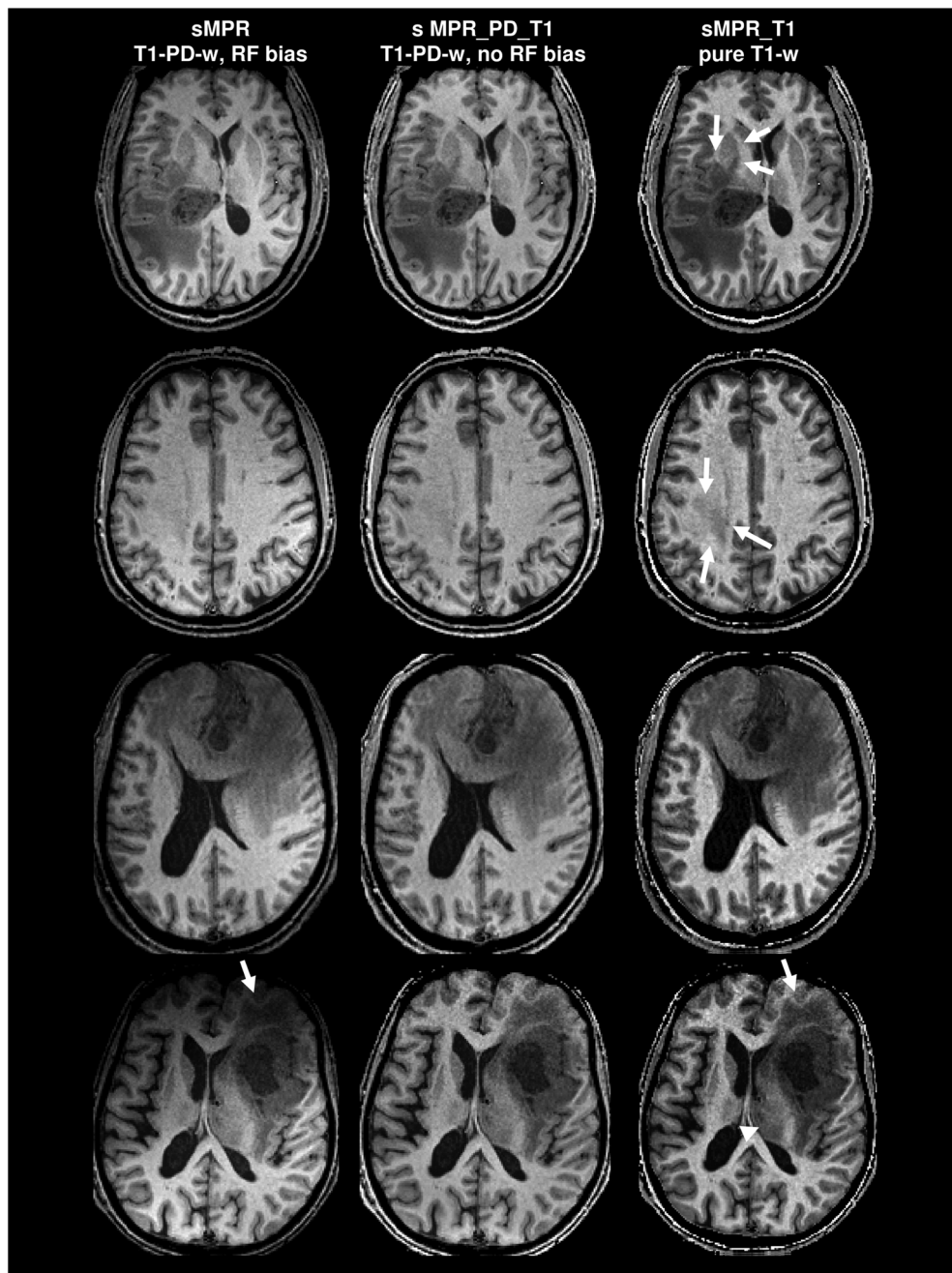


Figure 3. Single slices of the synthetic magnetization-prepared rapid acquisition of gradient echoes (MP-RAGE) anatomies (arrangement identical to Fig. 2) for four patients, demonstrating the detectability of tumor edema. The anatomies with pure T_1 weighting (last column) always provide the best visibility of edema (arrows). sMPR, synthetic MP-RAGE with proton density (PD) T_1 weighting and radiofrequency (RF) bias; sMPR_PD_T1, synthetic MP-RAGE with PD T_1 weighting without RF bias; sMPR_T1, synthetic MP-RAGE with pure T_1 weighting.

Although there are no clear-cut margins between infiltrative gliomas and normal brain (5,27,28), the respective MRI findings crucially influence clinical decisions regarding tumor resectability. For the examples in Fig. 2, sMPR_T1 clearly shows infiltration of the thalamus, hypothalamus and/or IC, informing the surgeon that a complete tumor resection is not feasible.

Conventional MRI protocols pose the problem that tumors and edema are best visualized on T_2 -weighted and FLAIR images (4,27–29) or contrast-enhanced T_1 -weighted images for the visualization of tumor regions with impaired blood-brain barrier (27,30), whereas the brain anatomy is best depicted on T_1 -weighted anatomies, such as MP-RAGE (2,3). This requires

MRI protocols with multiple contrasts, posing the problems of extended scan durations, different volume coverage (2D versus 3D), different slice orientations, a lack of sequence standardization, and scanner hardware and software bias (30).

qMRI overcomes these problems by yielding reproducible and objective maps exclusively showing the value of one single tissue parameter per map (e.g. T_1 , T_2 , PD), rather than the mixed contrasts in standard images. Furthermore, these maps allow for the calculation of synthetic anatomies, facilitating retrospective contrast optimization without requiring additional scans. As a result of theoretical considerations and previous reports (6–8,31), it was assumed that T_1 weighting is best suited to

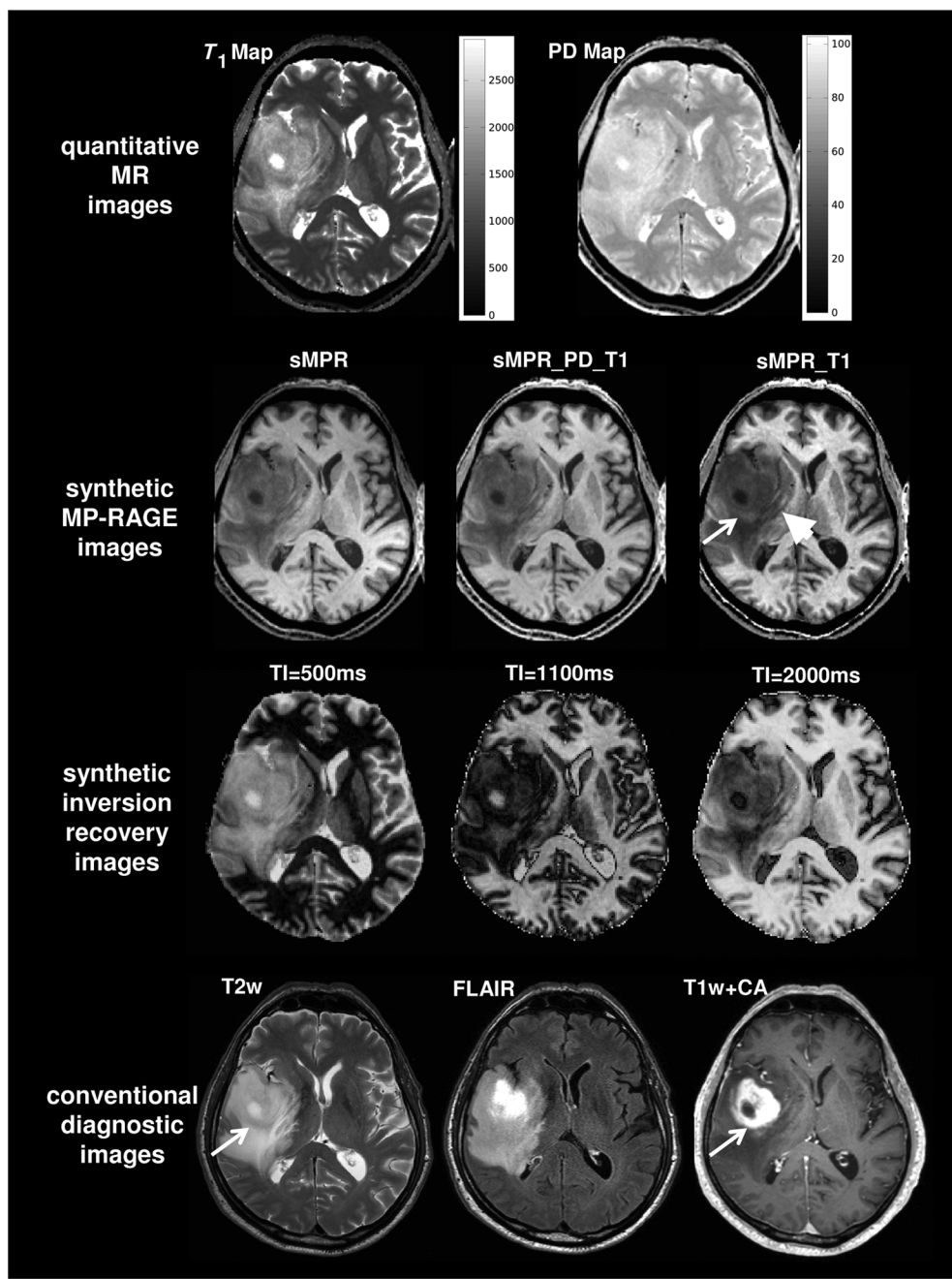


Figure 4. Selected slice from data acquired on a patient with a tumor in the temporal lobe and adjacent peritumoral edema. Imaging modalities are (from left to right): quantitative maps of T_1 and proton density (PD) (row 1), synthetic magnetization-prepared rapid acquisition of gradient echoes (MP-RAGE) images [sMPR, synthetic MP-RAGE with PD T_1 weighting and radiofrequency (RF) bias; sMPR_PD_T1, synthetic MP-RAGE with PD T_1 weighting without RF bias; sMPR_T1, synthetic MP-RAGE with pure T_1 weighting] (row 2), three examples of synthetic inversion recovery (IR) images calculated for inversion times (TIs) of 500, 1100 and 2000 ms (row 3), and the conventional diagnostic images T_2 -weighted, fluid-attenuated inversion recovery (FLAIR), and T_1 -weighted after contrast agent (CA) (row 4).

depict both brain anatomy and tumor tissue, as the water content is increased in tumor tissue and edema (6–8,32,33), yielding a concomitant T_1 prolongation. However, experience has shown that conventional T_1 -weighted data without contrast enhancement insufficiently depict tumor tissue. Previous studies have revealed that this is caused by increased PD values in tumor tissue, as PD is strongly correlated with T_1 (32–34), posing the problem of PD and T_1 inversely affecting the signal in T_1 -weighted sequences, thus mutually masking their effects (sMPR_PD_T1 and sMPR). In contrast, tumor visibility is strongly

improved in purely T_1 -weighted synthetic anatomies without PD bias (sMPR_T1).

Therefore, the results of this study encourage the use and further development of qMRI techniques and post-processing algorithms for brain tumor imaging. The qMRI data could also be used to calculate images employing various functions of T_1 and/or PD which provide improved contrast for different pathologies or allow a better delineation between healthy and pathological tissue; the calculation of purely T_1 -based synthetic IR images for different TIs is shown as a further example in Figs. 4

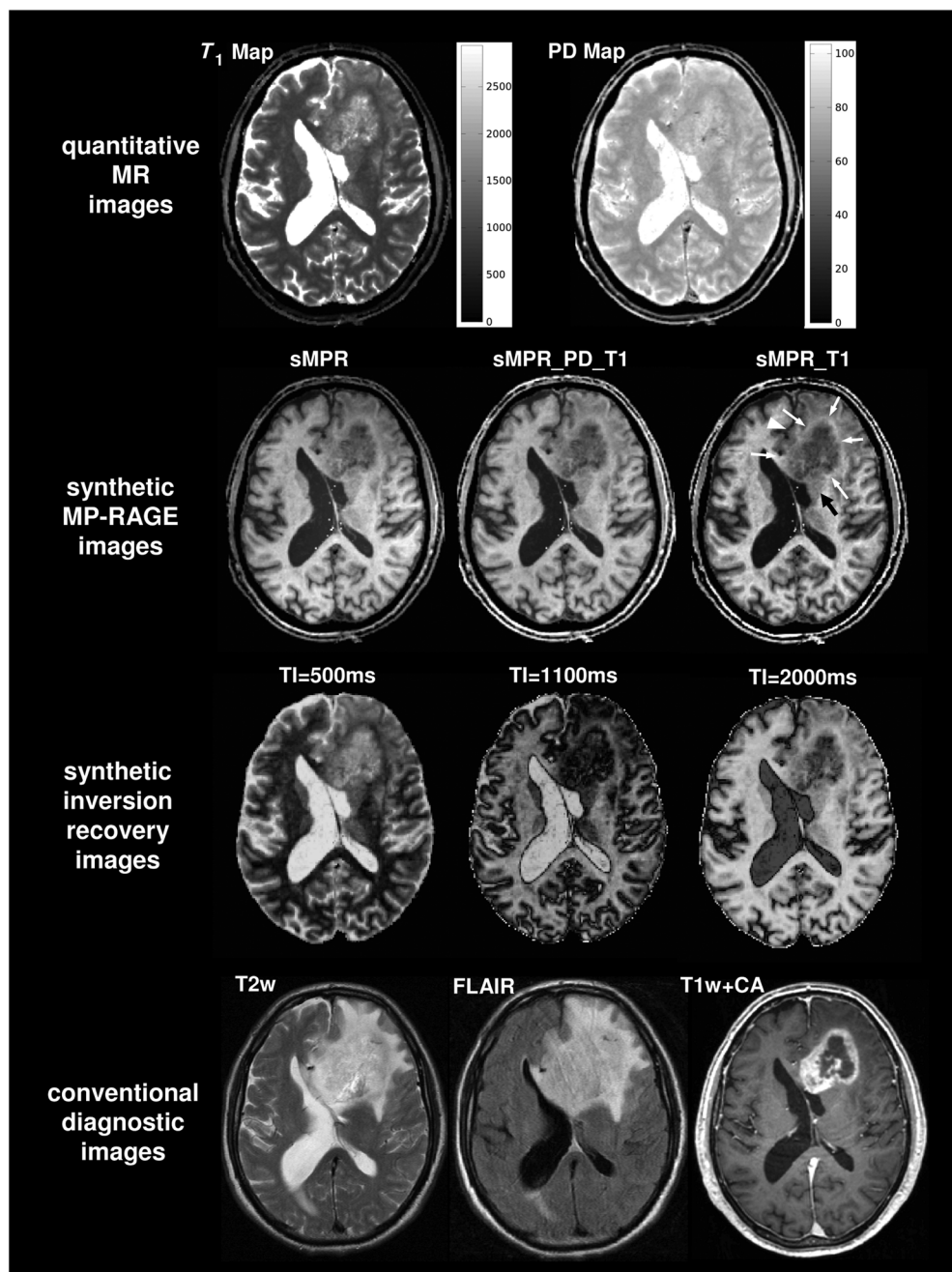


Figure 5. Selected slice from data acquired on a patient with a glioblastoma in frontal white matter (WM) that infiltrates the corpus callosum and is surrounded by edema. The tumor center is necrotic. Imaging modalities are (from left to right): quantitative maps of T_1 and proton density (PD) (row 1), synthetic magnetization-prepared rapid acquisition of gradient echoes (MP-RAGE) images (sMPR, synthetic MP-RAGE with PD T_1 weighting and radio-frequency (RF) bias; sMPR_PD_T1, synthetic MP-RAGE with PD T_1 weighting; sMPR_T1, synthetic MP-RAGE with pure T_1 weighting) (row 2), three examples of synthetic inversion recovery (IR) images calculated for inversion times (TIs) of 500, 1100 and 2000 ms (row 3), and the conventional diagnostic images T_2 -weighted fluid-attenuated inversion recovery (FLAIR), and T_1 -weighted after contrast agent (CA) (row 4).

and 5. Further applications of qMRI have already been shown for T_2 and T_2' mapping (35–39). In addition, considering that tissue T_1 is shortened after CA accumulation, the calculation of T_1 difference maps (before/after CA application) is likely to improve and objectify the detection of areas with impaired blood–brain barrier (40).

The problem with synthetic anatomies is the fact that the scan duration for the underlying qMRI techniques is longer than for classical anatomical imaging, at least if similar SNR and CNR levels are to be achieved. As an example, in a study performed

on patients with multiple sclerosis (11), the CNR between lesions and surrounding tissue was 11% higher in MP2-RAGE relative to standard MP-RAGE, but the acquisition time was increased by a factor of 2.21. In a study using the VFA technique (15), the synthetic data displayed an average CNR increase of 37%, but the reference standard anatomy was the T_1 -weighted dataset forming part of the VFA technique, i.e. scanned at half the acquisition time.

The purpose of the study on healthy subjects was to systematically compare acquired and synthetic MP-RAGE data, using

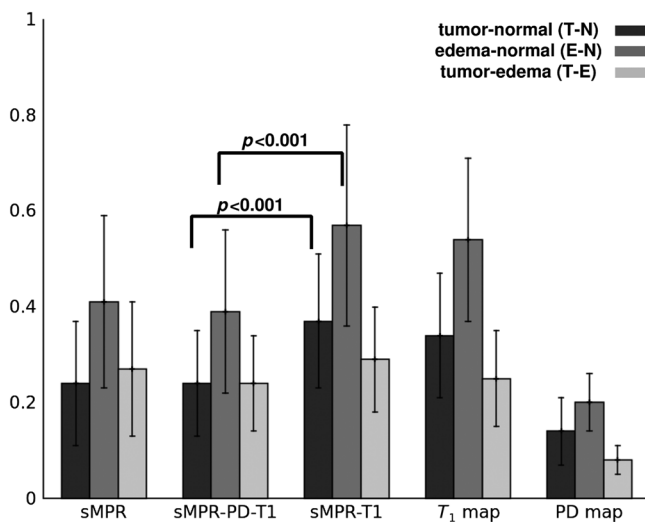


Figure 6. Average optical contrast values for all three synthetic anatomies and the quantitative T_1 and proton density (PD) map between tumor and surrounding normal tissue (T-N), edema and surrounding normal tissue (E-N), and tumor and edema (T-E). For T-N and E-N, sMPR_T1 provides a significantly higher optical contrast relative to the anatomies with PD T_1 weighting (sMPR and sMPR_PD_T1). For T-E, there are no significant differences. Values for the T_1 map are similar to sMPR_T1 (ca. 10% lower), whereas the PD map shows the lowest contrast. sMPR, synthetic magnetization-prepared rapid acquisition of gradient echoes (MP-RAGE) with PD T_1 weighting and radiofrequency (RF) bias; sMPR_PD_T1, synthetic MP-RAGE with PD T_1 weighting without RF bias; sMPR_T1, synthetic MP-RAGE with pure T_1 weighting.

similar scan durations (9 min 6 s versus 9 min 48 s). The results show that the synthetic anatomies accounting for all parameters (T_1 , PD, RF coil bias) match the acquired anatomies extremely well (Fig. 1), with only minor losses in quality: the SNR is reduced, but still attains about 80–90% of the SNR in the acquired anatomies. In contrast, the synthetic anatomies accounting only for T_1 suffer an SNR reduction by about 45–50%. However, they maintain a high CNR as they display a considerably higher optical contrast as the compromising influence of PD is removed.

There are two main reasons for the good performance of the synthetic data. First, in magnetization-prepared sequences, such as MP-RAGE, low flip angles and/or data filtering must be chosen to avoid the deleterious effect of spin relaxation during the acquisition process on the point spread function, causing blurring (18). In contrast, the qMRI techniques described here are based on fast GE acquisitions performed in steady state, and so larger angles will not compromise the point spread function. Second, the VFA technique used in this study employs a multi-echo readout (20), giving rise to larger SNR and CNR values.

It should be noted that the calculation of the underlying PD and T_1 maps includes a correction for B_1 effects. In this study, actual B_1 mapping was performed with a duration of 53 s which adds to the acquisition time of the PD- and T_1 -weighted data (9 min 48 s). However, it has been shown that B_1 can also be obtained from VFA data without additional measurements (41): mapping of T_1 without B_1 correction yields an apparent value $T_1(\text{app}) = T_1 \cdot B_1^2$. Thus, if $1/T_1(\text{app})$ is used as an anatomical dataset and bias field corrected, the resulting bias is B_1^{-2} , from which B_1 can be obtained (41). The accuracy of this method has been reported to be about 4% (41), which would be fully sufficient for creating synthetic anatomies without RF bias.

The question arises as to why synthetic anatomies based only on T_1 have a lower SNR than the respective anatomies accounting for both T_1 and PD. The reason is that noise in the PD and T_1 maps is correlated as they are derived from the same images: overestimation of the local T_1 as a result of noise yields an over-correction of T_1 effects in the PD-weighted data and thus an overestimation of PD. This noise-induced simultaneous enhancement of T_1 and PD is partially compensated in synthetic anatomies based on both parameters, as they affect signal levels inversely. This compensatory effect is missing in synthetic anatomies based on T_1 only. However, these anatomies supply a superior optical contrast, yielding a better visibility of pathologies. The SNR still assumes values of about 33–43 in WM and 25 in GM, with a CNR of about 14–19 between WM and GM. These values match the quality of classical T_1 -weighted sequences as described for anatomical imaging of the brain (24,42).

Acknowledgements

We would like to thank Stephanie Lescher and Se-jong You for performing the visual rating.

This study was supported by the Bundesministerium für Bildung und Forschung (Brain Imaging Center Frankfurt, DLR 01GO0203), the Deutsche Forschungsgemeinschaft (ZA 233/1-1) and the LOEWE-Program ‘Neuronal Coordination Forschungsschwerpunkt Frankfurt’ (NeFF).

Oliver Bähr has served as a consultant for Roche, the European distributor of Bevacizumab, and has received travel grants from Roche.

REFERENCES

- Hajnal JV, Coene BD, Lewis PD, Baudouin CJ, Cowan FM, Pennock JM, Young IR, Bydder GM. High signal regions in normal white matter shown by heavily T2-weighted CSF nulled IR sequences. *J. Comput. Assist. Tomogr.* 1992; 16(4): 506–513.
- Mugler JP, Brookeman JR. Three-dimensional magnetization-prepared rapid gradient-echo imaging (3D MP RAGE). *Magn. Reson. Med.* 1990; 15(1): 152–157.
- Brant-Zawadzki M, Gillan GD, Nitz WR. MP RAGE: a three-dimensional, T_1 -weighted, gradient-echo sequence—initial experience in the brain. *Radiology* 1992; 182(3): 769–775.
- Iwama T, Yamada H, Sakai N, Andoh T, Nakashima T, Hirata T, Funakoshi T. Correlation between magnetic resonance imaging and histopathology of intracranial glioma. *Neurol. Res.* 1991; 13(1): 48–54.
- Kelly PJ, Daumas-Dupont C, Kispert DB, Kall BA, Scheithauer BW, Illig JJ. Imaging-based stereotactic serial biopsies in untreated intracranial glial neoplasms. *J. Neurosurg.* 1987; 66(6): 865–874.
- Englund E, Brun A, Larsson EM, Györffy-Wagner Z, Persson B. Tumours of the central nervous system. Proton magnetic resonance relaxation times T_1 and T_2 and histopathologic correlates. *Acta Radiol. Diagn. (Stockh.)* 1986; 27(6): 653–659.
- Hoehn-Berlage M, Bockhorst K. Quantitative magnetic resonance imaging of rat brain tumors: in vivo NMR relaxometry for the discrimination of normal and pathological tissues. *Technol. Health Care*, 1994; 2(4): 247–254.
- Neel H, Zilles K, Shah NJ. A new method for fast quantitative mapping of absolute water content in vivo. *Neuroimage*, 2006; 31(3): 1156–1168.
- de Moortele P-FV, Auerbach EJ, Olman C, Yacoub E, Uğurbil K, Moeller S. T_1 -weighted brain images at 7 Tesla unbiased for proton density, T_2^* contrast and RF coil receive B_1 sensitivity with simultaneous vessel visualization. *Neuroimage* 2009; 46(2): 432–446.
- Marques JP, Kober T, Krueger G, van der Zwaag W, de Moortele P-FV, Gruetter R. MP2RAGE, a self bias-field corrected sequence for improved segmentation and T_1 -mapping at high field. *Neuroimage* 2010; 49(2): 1271–1281.

11. Kober T, Granziera C, Ribes D, Browaeys P, Schluep M, Meuli R, Frackowiak R, Gruetter R, Krueger G. MP2RAGE multiple sclerosis magnetic resonance imaging at 3 T. *Invest. Radiol.* 2012; 47(6): 346–352.
12. Venkatesan R, Lin W, Haacke EM. Accurate determination of spin-density and T1 in the presence of RF-field inhomogeneities and flip-angle miscalibration. *Magn. Reson. Med.* 1998; 40(4): 592–602.
13. Volz S, Nöth U, Jurcoane A, Ziemann U, Hattingen E, Deichmann R. Quantitative proton density mapping: correcting the receiver sensitivity bias via pseudo proton densities. *Neuroimage* 2012; 63(1): 540–552.
14. Riederer SJ, Bobman SA, Lee JN, Farzaneh F, Wang HZ. Improved precision in calculated T1 MR images using multiple spin-echo acquisition. *J. Comput. Assist. Tomogr.* 1986; 10(1): 103–110.
15. Deoni SCL, Rutt BK, Peters TM. Synthetic T1-weighted brain image generation with incorporated coil intensity correction using DES-POT1. *Magn. Reson. Imaging*, 2006; 24(9): 1241–1248.
16. Hecht E. Fourier optics. In: Hecht E (ed.). *Optics*. Addison-Wesley Publishing Company: Reading, MA; 1987, p. 507.
17. Deichmann R, Haase A. Quantification of T1 values by SNAPSHOT-FLASH imaging. *J. Magn. Reson.* 1992; 96: 608–612.
18. Deichmann R, Good CD, Josephs O, Ashburner J, Turner R. Optimization of 3-D MP-RAGE sequences for structural brain imaging. *Neuroimage* 2000; 12(1): 112–127.
19. Tardif CL, Collins DL, Pike GB. Sensitivity of voxel-based morphometry analysis to choice of imaging protocol at 3 T. *Neuroimage* 2009; 44(3): 827–838.
20. Preibisch C, Deichmann R. T1 mapping using spoiled FLASH-EPI hybrid sequences and varying flip angles. *Magn. Reson. Med.* 2009; 62(1): 240–246.
21. Volz S, Nöth U, Rotarska-Jagiela A, Deichmann R. A fast B1-mapping method for the correction and normalization of magnetization transfer ratio maps at 3 T. *Neuroimage* 2010; 49(4): 3015–3026.
22. Preibisch C, Deichmann R. Influence of RF spoiling on the stability and accuracy of T1 mapping based on spoiled FLASH with varying flip angles. *Magn. Reson. Med.* 2009; 61(1): 125–135.
23. Volz S, Nöth U, Deichmann R. Correction of systematic errors in quantitative proton density mapping. *Magn. Reson. Med.* 2012; 68: 74–85.
24. Deichmann R, Schwarzbauer C, Turner R. Optimisation of the 3D MDEFT sequence for anatomical brain imaging: technical implications at 1.5 and 3 T. *Neuroimage* 2004; 21(2): 757–767.
25. Rees JH, Smirniotopoulos JG, Jones RV, Wong K. Glioblastoma multiforme: radiologic-pathologic correlation. *Radiographics* 1996; 16(6): 1413–1438.
26. Ananthnarayan S, Bahng J, Roring J, Nghiempahu P, Lai A, Cloughesy T, Pope WB. Time course of imaging changes of GBM during extended bevacizumab treatment. *J. Neurooncol.* 2008; 88(3): 339–347.
27. Watanabe M, Tanaka R, Takeda N. Magnetic resonance imaging and histopathology of cerebral gliomas. *Neuroradiology* 1992; 34(6): 463–469.
28. Tovi M. MR imaging in cerebral gliomas analysis of tumour tissue components. *Acta Radiol. Suppl.* 1993; 384: 1–24.
29. Essig M, Hawighorst H, Schoenberg SO, Engenhart-Cabillic R, Fuss M, Debus J, Zuna I, Knopp MV, van Kaick G. Fast fluid-attenuated inversion-recovery (FLAIR) MRI in the assessment of intraaxial brain tumors. *J. Magn. Reson. Imaging* 1998; 8(4): 789–798.
30. Ellingson BM, Kim HJ, Woodworth DC, Pope WB, Cloughesy JN, Harris RJ, Lai A, Nghiempahu PL, Cloughesy TF. Recurrent glioblastoma treated with bevacizumab: contrast-enhanced T1-weighted subtraction maps improve tumor delineation and aid prediction of survival in a multicenter clinical trial. *Radiology* 2014; 271(1): 200–210.
31. Ngo FQ, Bay JW, Kurland RJ, Weinstein MA, Hahn JF, Glassner BJ, Woolley CA, Dudley AW, Ferrario CM, Meaney TF. Magnetic resonance of brain tumors: considerations of imaging contrast on the basis of relaxation measurements. *Magn. Reson. Imaging* 1985; 3(2): 145–155.
32. Just M, Thelen M. Tissue characterization with T1, T2, and proton density values: results in 160 patients with brain tumors. *Radiology* 1988; 169(3): 779–785.
33. Fatourou PP, Marmarou A. Use of magnetic resonance imaging for in vivo measurements of water content in human brain: method and normal values. *J. Neurosurg.* 1999; 90(1): 109–115.
34. Fatourou PP, Marmarou A, Kraft KA, Inao S, Schwarz FP. In vivo brain water determination by T1 measurements: effect of total water content, hydration fraction, and field strength. *Magn. Reson. Med.* 1991; 17(2): 402–413.
35. Saitta L, Heese O, Förster A-F, Matschke J, Siemonsen S, Castellan L, Westphal M, Fiehler J, Goebell E. Signal intensity in T2' magnetic resonance imaging is related to brain glioma grade. *Eur. Radiol.* 2011; 21(5): 1068–1076.
36. Hattingen E, Jurcoane A, Bähr O, Rieger J, Magerkurth J, Anti S, Steinbach JP, Pilatus U. Bevacizumab impairs oxidative energy metabolism and shows antitumoral effects in recurrent glioblastomas: a ³¹P/¹H MRSI and quantitative magnetic resonance imaging study. *Neuro Oncol.* 2011; 13(12): 1349–1363.
37. Hattingen E, Jurcoane A, Daneshvar K, Pilatus U, Mittelbronn M, Steinbach JP, Bähr O. Quantitative T2 mapping of recurrent glioblastoma under bevacizumab improves monitoring for non-enhancing tumor progression and predicts overall survival. *Neuro Oncol.* 2013; 15(10): 1395–1404.
38. Ellingson BM, Cloughesy TF, Lai A, Nghiempahu PL, Lalezari S, Zaw T, Mottevalibashinaeini K, Mischel PS, Pope WB. Quantification of edema reduction using differential quantitative T2 (DQT2) relaxometry mapping in recurrent glioblastoma treated with bevacizumab. *J. Neurooncol.* 2012; 106(1): 111–119.
39. Tóth V, Förtschler A, Hirsch NM, den Hollander J, Kooijman H, Gempt J, Ringel F, Schlegel J, Zimmer C, Preibisch C. MR-based hypoxia measures in human glioma. *J. Neurooncol.* 2013; 115(2): 197–207.
40. Jurcoane A, Wagner M, Schmidt C, Mayer C, Gracién R-M, Hirschmann M, Deichmann R, Volz S, Ziemann U, Hattingen E. Within-lesion differences in quantitative MRI parameters predict contrast enhancement in multiple sclerosis. *J. Magn. Reson. Imaging* 2013; 38(6): 1454–1461.
41. Weiskopf N, Lutti A, Helms G, Novak M, Ashburner J, Hutton C. Unified segmentation based correction of R1 brain maps for RF transmit field inhomogeneities (UNICORT). *Neuroimage* 2011; 54: 2116–2124.
42. Stöcker T, Shah NJ. MP-SAGE: a new MP-RAGE sequence with enhanced SNR and CNR for brain imaging utilizing square-spiral phase encoding and variable flip angles. *Magn. Reson. Med.* 2006; 56(4): 824–834.